2D Materials

PAPER

RECEIVED
1 September 2025

REVISED
11 November 2025

ACCEPTED FOR PUBLICATION
6 January 2026

PUBLISHED
19 February 2026

Wide-field hyperspectral optical microscopy for rapid characterization of two-dimensional semiconductors and heterostructures

Zhenghan Peng[1], Adeyemi Uthman[1], Zhepeng Zhang[1], Anh Tuan Hoang[1], Xiang Zhu[1], Eric Pop[1,2,3] and Andrew J Mannix[1,4,*]

[1] Department of Materials Science & Engineering, Stanford University, Stanford, CA 94305, United States of America
[2] Department of Electrical Engineering, Stanford University, Stanford, CA 94305, United States of America
[3] Department of Applied Physics, Stanford University, Stanford, CA 94305, United States of America
[4] Stanford Institute for Materials and Energy Sciences, SLAC National Accelerator Laboratory, Menlo Park, CA 94025, United States of America
[*] Author to whom any correspondence should be addressed.

E-mail: ajmannix@stanford.edu

Keywords: hyperspectral microscopy, differential reflectance, high-throughput characterization, two-dimensional transition-metal dichalcogenides, heterostructures

Abstract

Electronic and optoelectronic applications of two-dimensional (2D) semiconductors demand precise control over material quality, including thickness, composition, doping, and defect density. Conventional benchmarking methods (e.g. charge transport, confocal mapping, electron or scanning probe microscopy) are slow, perturb sample quality, or involve trade-offs between speed, resolution, and scan area. To accelerate assessment of 2D semiconductors, we demonstrate a broadband, wide-field hyperspectral optical microscope for 2D materials that rapidly captures a spatial-spectral data cube within seconds. The data cube includes x–y spatial coordinate (a 300 × 300 μm^2 field, with ~1 μm resolution) and a selectable wavelength range between 200 nm to 1100 nm at each pixel. Using synthesized films and heterostructures of transition metal dichalcogenides (MoS_2, WS_2, $V_xW_{1-x}S_2$, and WSe_2), we show that this cost-effective technique detects spectral fingerprints of material identity, doping, grain boundaries, and alloy composition, and enables advanced analysis, including unsupervised machine learning for spatial segmentation.

1. Introduction

Two-dimensional (2D) semiconductors such as the transition metal dichalcogenides (TMDCs, e.g. MoS_2, WS_2, $MoSe_2$, or WSe_2) exhibit appealing properties including good charge transport in sub-nanometer thin films and strong excitonic effects in their optical response, enabling applications in electronic and photonic devices [1–4]. Additionally, lateral and vertical heterostructures result in an even greater variety of interesting properties based on carrier confinement, interlayer charge transfer, moiré superlattices, and other novel effects [5–8]. Early experiments used micrometer-scale TMDC flakes produced by micromechanical exfoliation, limiting device area and scalability. This has motivated significant efforts to synthesize TMDCs deterministically with high-quality over large areas, and to integrate them into heterostructures. However, despite significant progress in the growth of monolayer and few-layer films of TMDCs by techniques like atomic layer deposition [9], solid-source chemical vapor deposition (SS-CVD) [10–12], metal–organic CVD (MOCVD) [13, 14], molecular beam epitaxy [15–17], or metal film chalcogenization [18, 19], these techniques do not presently meet the needs of advanced technology nodes, and in many cases have higher defect density than the best exfoliated monolayer films. As a result, the scalable synthesis of high-quality films remains a bottleneck, and many researchers continue to rely upon micromechanical exfoliation.

Optimizing the electrical, optical, and mechanical properties of thin-film TMDCs and other 2D semiconductors requires accurate feedback on sample quality, defined by minimal defects, uniform composition and crystal structure, and precisely controlled doping. Although fabricating and measuring transistors can quantify some key aspects of film quality, the process is time consuming and electrical measurements do not uniquely identify the concentration, location, or type of defects. Additionally, doping or degradation may occur during fabrication [20, 21], which complicates the interpretation of growth quality based on device measurements. Altogether, the slow rate of device fabrication and interpretation is not well-matched to provide timely feedback on high throughput of SS-CVD or MOCVD, making it impractical to fabricate and test devices from every growth batch. Therefore, rapid assessment of crystalline, interfacial, and electrical quality is essential for guiding synthesis optimization and screening samples for further fabrication or advanced measurements.

Many techniques characterize TMDCs after synthesis, but no rapid, widely accepted method exists for overall sample quality assessment. Techniques like scanning or transmission electron microscopy [22], scanning probe microscopy [23–25], and confocal optical spectroscopy [26] provide valuable insights but are limited by small fields of view, low throughput, or insufficient sensitivity to the electronic or chemical states. Additionally, individual confocal photoluminescence (PL) or Raman spectra typically measure a small ($\sim$1 μm^2) area, and therefore acquisition over many points is needed to determine which data are representative and to identify local fluctuations. Chemically sensitive techniques like x-ray photoelectron spectroscopy provide improved composition information but suffer from poor spatial resolution and require high-vacuum conditions, leading to longer measurement times. This underscores the need for a swift, spatially-precise, and non-invasive technique to assess material quality and identify key properties. Optical reflectance, which is sensitive to the electronic structure of TMDCs, can be rapidly measured using hyperspectral optical microscopy to sequentially acquire wavelength-resolved 2D images [27, 28], yet its potential for high-throughput 2D semiconductor characterization remains underexplored.

Here, we demonstrate an optimized hyperspectral optical microscopy technique for rapid characterization of 2D materials and heterostructures (2D-HOM), offering good spatial resolution ($<$1 μm) and sensitivity to doping and defects over large areas ($\sim$300 $\times$ 300 μm^2) with acquisition times ranging from tens of seconds to several minutes. This system uses wide-field, spectrally-resolved reflectance imaging in a custom optical microscope, spanning wavelengths from 1100 to 200 nm (photon energies of 1.15–6.2 eV) to capture electronic transitions in TMDCs such as MoS_2, WS_2, and WSe_2. This method can distinguish between different TMDCs on a substrate, detect spatial variations in doping, identify grain boundaries (GBs), map alloy composition, and quickly generate multidimensional data sets for further analysis using machine learning (ML) [29].

2. Results and discussions

The 2D-HOM system can be assembled using off-the-shelf optical components. Figure 1(a) illustrates the 2D-HOM setup showing both the front view and the side view. A commercial tunable light source (Sciencetech TLS-55-X300) directs light from a Xe lamp into a ¼ meter monochromator, outputting a single wavelength within the range of 200–2000 nm. The monochromator's output provides good spectral resolution, typically 0.5–1 nm full width at half-maximum on the output light. The light is guided by a multimode, solarization-resistant silica fiber and launched into the microscope illumination arm using a reflective collimator. The microscope imaging path is configured for epi-reflectance imaging of opaque samples and uses reflective components to remove chromatic aberration.

The 2D-HOM captures a sequence of reflectance images within the spectral range of 1100–200 nm, which is determined by the response of our backside-illuminated silicon CMOS camera (corresponding to energies of 1.15–6.2 eV). This yields a three-dimensional (3D) data cube R (x, y, λ) as shown on the left of figure 1(b). The differential reflectance (DR), which is sensitive to a material's electronic structure [31, 32], is calculated from the reflectance of the 2D material regions of interest on the sample (R_{2D}) and the reflectance of the substrate ($R_{substrate}$), $\frac{\Delta R}{R} = \frac{R_{2D} - R_{Substrate}}{R_{Substrate}}$ illustrated on the right of figure 1(b). High resolution point spectroscopy across a wide spectral range (hyperspectral) have already been performed to capture wide-field images [33] and determine layer number of the TMDs [34], demonstrating the usefulness of theses spectra. Because the system records the full field of view at each wavelength, a stack of wavelength-selective reflectance maps over the entire sample can be acquired in seconds to minutes. This contrasts with PL mapping of the same region, which typically requires point- or line-based acquisition to reach comparable spatial coverage.

The DR spectra acquired from the 2D-HOM are highly sensitive to the electronic structure of 2D semiconductors. Representative spectra from synthetic CVD monolayers of WS_2 (figure 1(c)), MoS_2 (figure 1(d)), and WSe_2 (figure 1(e)) exhibit excitonic

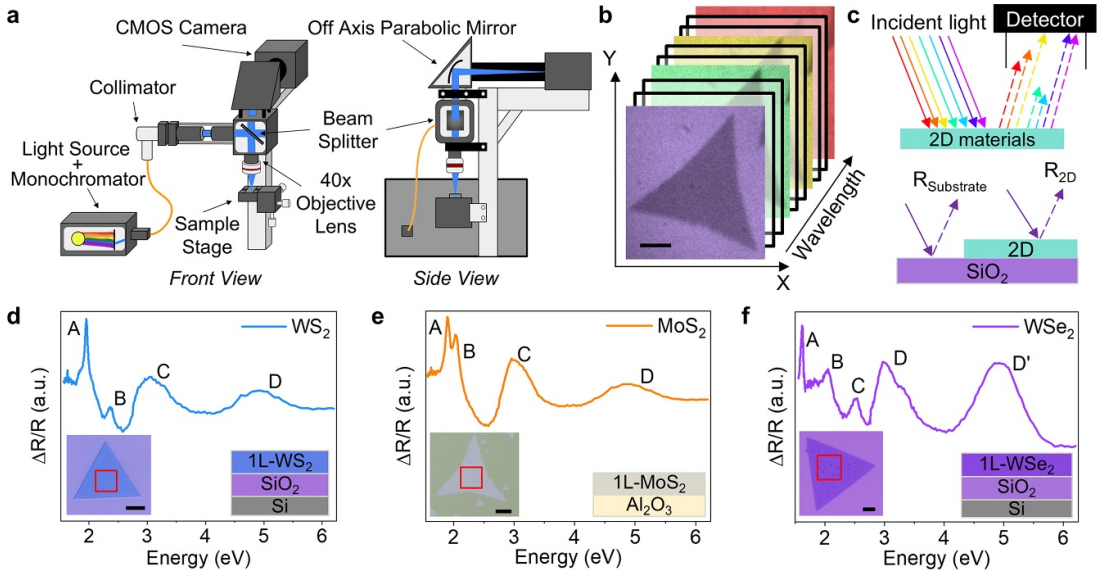

Figure 1. Design and demonstration of hyperspectral optical microscope for 2D materials (2D-HOM). (a) Schematic of the home-built 2D-HOM system, consisting of: (1) tunable light source with monochromator, (2) beam-splitting and imaging optics, and (3) CMOS camera. (b) Schematic of the data cube collected under different wavelengths, where the scale bar is 10 μm. (c) Schematics of the reflection that occurs on the surface of the sample, and the definition of $R_{substrate}$ and R_{2D}. (d)–(f) Differential reflectance (DR) spectra of hybrid-MOCVD [30] (Hy-MOCVD) grown monolayer (1L) WS_2, MoS_2, and solid-source CVD grown monolayer (1L) WSe_2. Spectra are collected by averaging signals in the middle region of the materials (as shown in the red boxes). The left insets are optical microscope images with scale bars of 5 μm. The right insets are schematic cross-sectional diagrams of the measured sample.

peak features, characteristic of their specific electronic band structure [35, 36]. The two lowest energy peaks are the A and B excitons, originating from spin–orbit splitting of the valence band in monolayer TMDCs [37]. The A exciton peak corresponds to the direct band gap transitions at the K point in the Brillouin zone [35–37]. (This is the optical band gap, which is smaller than the electronic gap by the energy of the A exciton.) This peak is typically prominent and plays a major role in our 2D-HOM analysis, although in principle any of the exciton peaks can provide information on the electronic structure. The B exciton peak originates from a similar K-point direct transition from the lower energy level of the spin–orbit split valence band and occurs at slightly higher energies (approximately + 400 meV, + 150 meV and + 440 meV for WS_2, MoS_2, and WSe_2 respectively). The higher-energy exciton peaks are generally associated with optical transitions involving band nesting (C exciton) [38–40] and higher energy transitions near the Γ point (D exciton) [41–43]. In WSe_2, the spin-split valence band yields an additional high-energy D′ exciton [44]. These features provide more nuanced information about the band structure, but further study is required to assess their value for material quality benchmarking. The wide energy range of our system (1.15–6.2 eV) enables us to probe many material systems, including multilayers and heterostructures [45].

Electronic structure is a function of composition and is modified by local defects and strain, and 2D-HOM is capable of distinguishing variations and inhomogeneities in the electronic structure which arise from these factors. This can be applied to study impactful challenges in the processing and optimization of 2D semiconductors. For example, substitutional doping requires controlled changes in composition, such as by introducing vanadium as an acceptor in WS_2 [46, 47]. Vanadium-doped WS_2 samples ($V_xW_{1-x}S_2$) with nominal doping concentration x ranging from 0.4% to 30% V were prepared using hybrid MOCVD [30]. As shown by the green curves in figure 2(a), the DR spectra exhibit progressively broadened and redshifted A exciton peaks with increasing vanadium concentration, while the B exciton peaks diminish in prominence. Similarly, the PL spectra (purple in figure 2(a)) also broaden and redshift as vanadium content rises. These spectral changes arise from changes to the WS_2 electronic structure due to vanadium doping, which increases hole concentration and the density of acceptor states near the valence-band edge [48]. Consequently, both DR and PL spectra experience red shifting and broadening due to narrower bandgap transition energies from excitations involving acceptor states, and PL intensity is quenched by the rise in free holes [49, 50]. Although the PL spectra in figure 2 exhibit higher SNR than the corresponding $\Delta R/R$ spectra, the $\Delta R/R$ maps capture the same doping-dependent spectral shifts and spatial inhomogeneities. Because $\Delta R/R$ is acquired in a wide-field configuration, the full area can be mapped at multiple photon energies

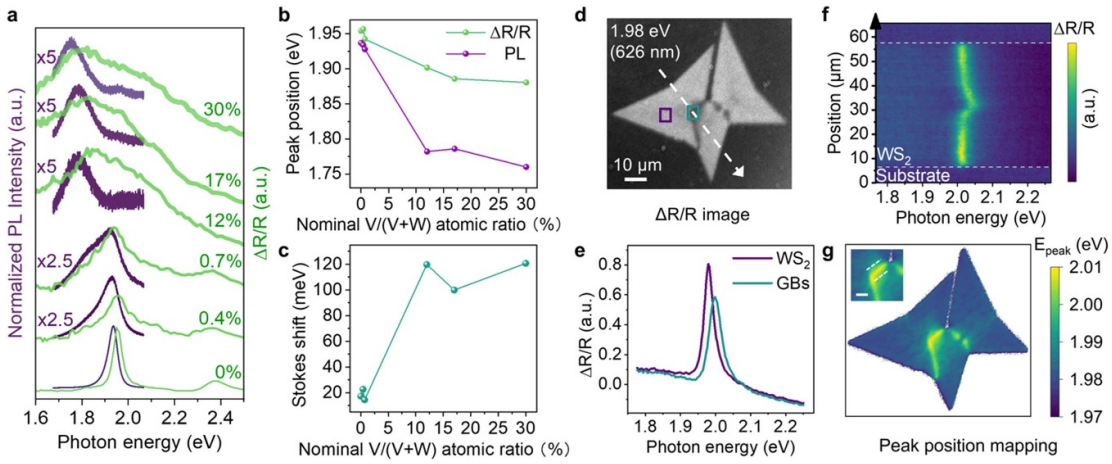

Figure 2. Analysis of doping and defects using 2D-HOM. (a) Differential reflectance (DR) and photoluminescence (PL) spectra, in green and purple respectively, of monolayer undoped pure WS_2 and V-doped WS_2 ($V_xW_{1-x}S_2$) with different nominal doping concentrations (x) from 0.4% to 30%. For better comparison, the intensity of the PL spectra for $x = 12\%$, 17% and 30% are multiplied by 5, and spectra for $x = 0.4\%$ and 0.7% are multiplied by 2.5. (b) PL and $\Delta R/R$ peak positions as a function of nominal V-doping concentration x. (c) Stokes shift as a function of nominal V-doping concentration x. (d) DR image (each pixel has a value of calculated $\frac{\Delta R}{R}$) of a WS_2 island with grain boundaries (GBs) under 1.98 eV (626 nm) illumination. (e) DR spectra of the selected WS_2 region (purple square) and GBs (darker green square). (f) Line profile along the slice direction shown as white dotted arrow in (d). (g) 2D mapping of the peak positions (fitted using Lorentz function) of the spectra; inset is the magnified GB region with a scale bar of 5 μm.

significantly faster than with PL mapping, which typically requires point- or line-scanning to achieve similar spatial coverage.

Additionally, we correlated doping concentration with defect-related Stokes shifts [51]. As depicted in figure 2(b), the peak positions of both DR and PL decrease with higher nominal vanadium ratios. The Stokes shift (E_{DR}–E_{PL}) shown in figure 2(c) increases with x, reaching up to 121 meV at 30% V. This trend is consistent with literature where the Stokes shift increases from ~40 meV for pure WS_2 to 55 meV for 8% V doped WS_2, indicating that larger Stokes shifts arise from significant doping, suggesting that emission is dominated by additional trapping (acceptor) states [52, 53]. The 2D-HOM can detect dopant levels as low as 0.4%, demonstrating sufficient sensitivity for applications such as materials metrology to improve material synthesis process.

We also quantitatively visualized the effects of GBs, which create strain and one-dimensional lattice defects that modify the local electronic structure [54, 55]. As shown in figure 2(d), the DR image of WS_2 at 1.98 eV (626 nm) reveals distinct optical contrast between the WS_2 regions and the GBs. Such differentiation is challenging to achieve with standard optical microscopy but is important in assessing the quality of a film, especially when polycrystalline edges and facets are not visible. Spectra in figure 2(e) are averaged from the highlighted areas in figure 2(d) and demonstrate a blue shift and a decrease in amplitude of the DR signal for the A exciton near the GBs. The blue shift is consistent with broadening of the bandgap, which can be attributed to the strain that occurs at the GBs regions due to lattice mismatch [56]. Theoretical models suggest that the conduction band minimum is raised in misoriented GBs under less than 3% compressive strain, increasing the bandgap [57]. This shift of ~50 meV is consistent with a ~0.6% local compressive strain at the GBs [58–60]. Additionally, 2D-HOM provides detailed spatial characterization of defective regions; the line profile in figure 2(f) shows a gradual peak shift from 2 eV to approximately 2.05 eV. By fitting Lorentzian peaks for individual pixels, we obtain a 2D map of A exciton energy in figure 2(g), which demonstrates that GB effects extend around 5 μm beyond the boundary. Evidently, 2D-HOM is capable of assessing the quality of synthetic materials by detecting doping or defects, and may be useful to track perturbations introduced by processing and fabrication [61].

Local variations in composition can be inferred through 2D-HOM analysis. To illustrate this, we analyze an alloyed lateral heterostructure sample with a composition of $W_\alpha Mo_{1-\alpha}S_2$. The sample's profile is depicted in the lower right of figure 3(b), with regions 1, 2, and 3 labeled on the right. Under optical microscope (figure 3(a)), the alloy appears as a continuous triangle with minimal internal contrast, although a subtle central triangular region is discernible. The DR image (figure 3(b)) at 1.98 eV (626 nm) clearly visualizes three distinct regions—outer (R1), middle (R2), and inner (R3)—with varying optical contrast.

DR spectra for each region are shown in figure 3(c) alongside pure WS_2 and MoS_2 spectra

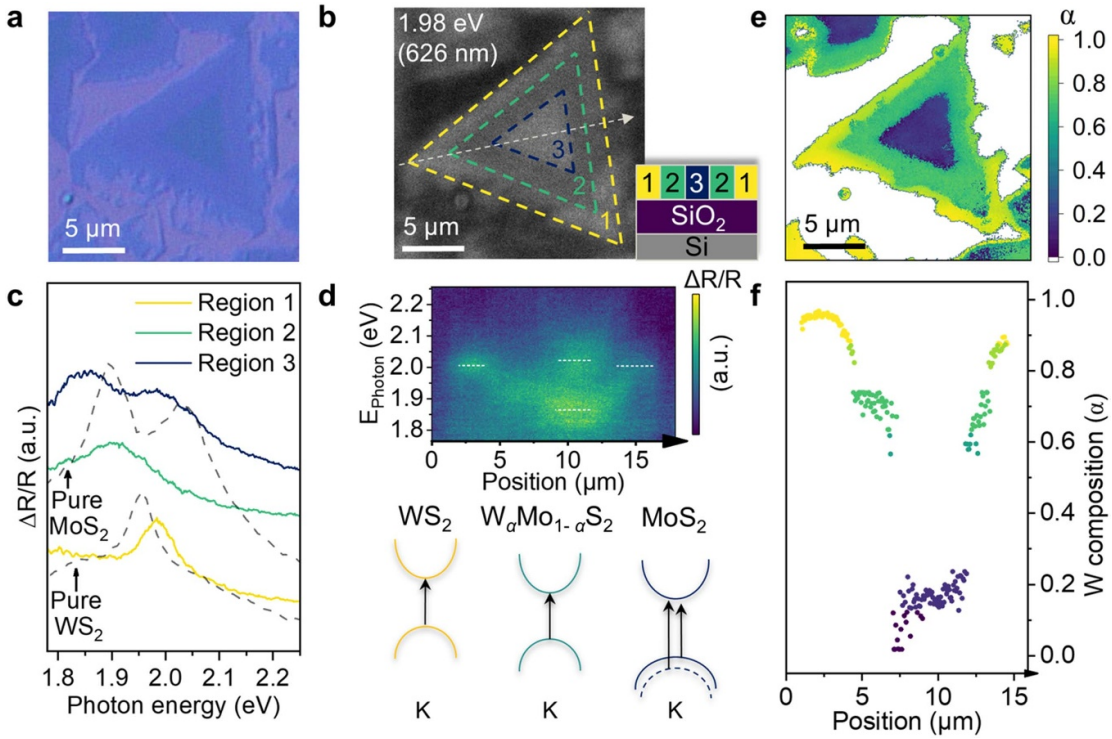

Figure 3. Analysis of chemical composition using 2D-HOM. (a) The optical microscope image of a $W_\alpha Mo_{1-\alpha}S_2$ alloy sample transferred onto a SiO_2/Si substrate. (b) The differential reflectance (DR) image of the alloy sample at 1.98 eV (626 nm). Alongside is the profile structure of the sample. (c) $\Delta R/R$ spectra of the alloy regions 1, 2 and 3 labeled in (b) compared with reference undoped, and unalloyed WS_2 (bottom, dotted) and MoS_2 (top, dotted) spectra measured on the same 2D-HOM system. (d) The upper part is the line profile of the slice direction shown as white dotted arrow in (b). The lower part illustrates the possible band structure changes in the alloy sample. (e) 2D mapping of *W* composition (α) of the same triangle in (a). (f) Calculated *W* composition (α) line profile along slice direction marked by the arrow in (b).

(dashed lines). R1 exhibits an A exciton peak at ∼2 eV which resembles pure WS_2, and R3 displays A and B exciton peaks at 1.86 eV and 2 eV, respectively, which resemble pure MoS_2 [36]. The middle, R2, exhibits a peak around 1.9 eV, which is consistent with a $W_\alpha Mo_{1-\alpha}S_2$ alloy. A DR line profile, shown in figure 3(d), was extracted from the white dotted line in figure 3(b), illustrating the gradual shift in the A exciton position from R1 to R2, and the emergence of a second peak, consistent with the MoS_2-like B exciton, in the transition from R2 to R3 [62, 63].

Using this electronic structure information, we inferred the *W* concentration (α in $W_\alpha Mo_{1-\alpha}S_2$) along the line profile (figure 3(f)) and in a 2D map (figure 3(e)) by interpolating between the measured WS_2 and MoS_2 A and B exciton peak positions, while considering the band bowing effect, $E_{W_\alpha Mo_{1-\alpha}S_2} = \alpha E_{WS_2} + (1-\alpha)E_{MoS_2} - b*\alpha(1-\alpha)$. The b in the equation is the bowing factor, 0.25 eV and 0.19 eV for A and B excitons of TMDs respectively [64]. Along the slice direction (white dashed line) in figure 3(b), the *W* composition (α) decreases from $\alpha = 0.95$ near the corner to ∼0.1 at the center of the triangle, then rises again to ∼0.9 near the edge. The 2D mapping further highlights this compositional variation from R1 (yellow) to R3 (dark blue), reflecting a decrease in *W* composition (α). These results align with our previous finding that growth of alloys with a Mo:W precursor ratio of 1:2 typically exhibits a MoS_2-like core and a WS_2-like shell [30]. 2D-HOM adds the capability for quick and quantitative spatial composition analysis, which is a useful addition to existing characterization techniques for 2D heterostructure growth. This alloy sample demonstrates that 2D-HOM can quantitatively distinguish chemical compositions in a lateral heterostructure using the extracted spectral information. Similarly high spatial resolution DR mapping is expected to be useful for large-area analysis of materials quality, inhomogeneity, and *in-situ* composition changes during synthesis.

Beyond the manual spectral analysis outlined above, the 2D-HOM system provides a rich combination of spatial and spectral data that can be mined for further information using emerging artificial intelligence (AI) or ML techniques [29]. As an illustrative example where the categorization capabilities of AI/ML algorithms prove useful, we studied a WS_2/MoS_2 vertical heterostructure. As shown in figures 4(a) and (f), we fabricated the WS_2/MoS_2 vertical heterostructure by transferring Hy-MOCVD-grown thin films (see methods section) and acquired a hyperspectral DR dataset (figure 4(b)). We then

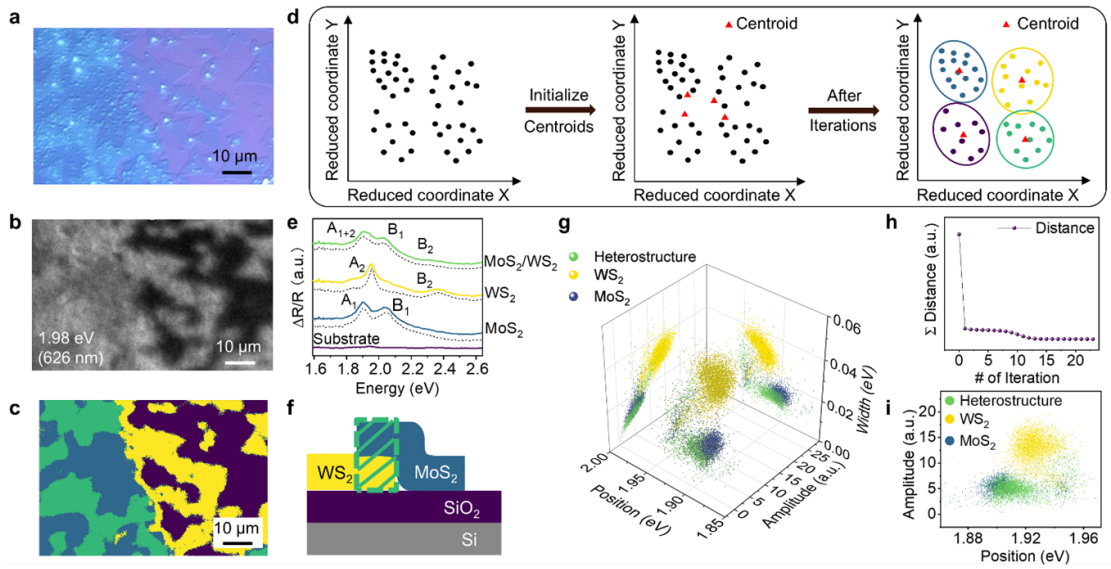

Figure 4. Machine learning for the analysis of heterostructures with 2D-HOM. (a) Optical microscope image of WS_2/MoS_2 vertical heterostructure with a schematic profile shown in (f). (b) Differential reflectance image of the heterostructure at 1.98 eV. (c) Image formed by segmenting the heterostructure region via *K*-means clustering, using the 3D DR data cube as the input. (d) Illustration of *K*-means clustering algorithm. The red triangles demonstrate different centroids. (e) Plot of the characteristic exemplar spectra extracted for each of the regions defined by *K*-means clustering. Corresponding dotted lines are the manually selected spectra of materials region. (g) 3D scatterplot of parameters for peaks fitted to the A-exciton features of the individual spectra at each (*x*, *y*) coordinate. The data points are labeled with colors corresponding to their *K*-means cluster assignment. This 3D display indicates that clustering of the raw hyperspectral data accurately differentiates the individual sample regions. The left and right walls of the 3D plot area show projections of the scatterplot for the amplitude-width plane and the position-width plane, respectively. (h) Plot of changes in the summation distance from all points to the centroid as a function of the number of *K*-means clustering iterations, demonstrating convergence during the clustering process. (I) Plot of the fitted A-exciton peak parameters projected to the position-amplitude plane.

applied a *K*-means clustering algorithm (figure 4(d) and method section) directly to the heterostructure's 3D DR data cube, partitioning each pixel into one of the clusters based on its spectral characteristics according to their squared Euclidean distance to the cluster centroids. The centroids are updated iteratively until the cluster assignment converges.

We assigned four clusters to this system based on our prior knowledge of the input materials: WS_2, MoS_2, heterostructure regions, and bare substrate. The clustering results, shown in figure 4(c), categorize regions into four distinct clusters: purple (SiO_2 substrate), yellow (pure WS_2), dark blue (pure MoS_2), and green (WS_2/MoS_2 vertical heterostructure). Exemplar spectra of these four regions are shown in figure 4(e). The substrate spectrum is flat, while the peak positions of the WS_2 and MoS_2 spectra match expected values [36, 37]. The heterostructure spectrum features a broadened A exciton peak, representing a combination of MoS_2 (A_1) and WS_2 (A_2) excitons, and dual B exciton peaks corresponding to MoS_2 (B_1) and WS_2 (B_2). The asymmetry in the B_2 peak arises from the presence of the A_2 peak. This aligns with previous studies indicating that the total DR response of layered heterostructures can be modeled as a linear combination of their constituent layers [31]. Additionally, manually selected spectra for each region (excluding the substrate) are overlaid as black dotted lines in figure 4(e), further validating the clustering accuracy.

To further substantiate our clustering approach, figure 4(g) presents a 3D visualization of the clustering outcomes. For each pixel within the materials clusters, the A exciton peak (lowest energy) was fitted using a Lorentz function, extracting three parameters: peak position, amplitude and width, plotted in figure 4(g). The separation of the data points in the 3D view corroborates the effectiveness of the clustering. Figure 4(h) illustrates the total cumulative Euclidean distance between each data point and its corresponding centroid versus the number of iterations, demonstrating that the algorithm successfully converges by minimizing these distances.

The robustness of the clustering is evident in the peak position-amplitude plane in figure 4(i): although the overlapping peak positions of MoS_2 and the heterostructure would complicate traditional segmentation, the added dimensionality from clustering enables clear separation of these regions. This demonstrates the potential of 2D-HOM to leverage AI/ML for high-throughput characterization, enhancing the analysis of complex hyperspectral datasets and revealing subtle features that may escape manual interpretation [65]. While the present work focuses on establishing proof-of-concepts where optical responses can be better correlated with known

perturbations using ML, it lays the groundwork for future larger-scale ML-enabled studies aimed at *a priori*-free identification of different kinds of 2D materials and the heterogeneity within them.

3. Conclusion

In this study, we demonstrate that 2D-HOM enables rapid and versatile characterization of 2D materials across a broad spectral range, from the deep ultraviolet to near-infrared. By capturing rich 3D hyperspectral data sets, 2D-HOM enables identification of materials based on their spectral signatures and reveals spatial variations in composition or defect density. These capabilities make 2D-HOM a powerful platform for fast quality assessment and inhomogeneity detection. When integrated with AI/ML algorithms, 2D-HOM can accurately differentiate regions within complex heterostructures—a task that is challenging for conventional optical microscopes. Additional dimensions of contrast could be introduced through electrostatic gating [66, 67], photoexcitation [68], or wavelength-selective detection [69]. These results highlight the potential of 2D-HOM for high-throughput materials evaluation and support future advances in characterization and synthesis of 2D materials [70]. The 2D-HOM platform could evolve into a benchmarking approach within the 2D materials research community. Nevertheless, realizing this potential will necessitate the collection of extensive datasets from various kinds of 2D materials and the development of robust machine-learning models trained across multiple experimental conditions.

4. Methods

4.1. Materials growth

Monolayer WS_2, MoS_2, $W_\alpha Mo_{1-\alpha}S_2$ alloy, and *V*-doped monolayer WS_2 ($V_xW_{1-x}S_2$) were prepared with dip-coating Hy-MOCVD, as reported in our previous paper [30]. For the growth of monolayer WS_2 on the SiO2/Si substrate with a 100 nm SiO2 layer, ammonium metatungstate hydrate (AMT) and potassium hydroxide (KOH) solution (0.6 g + 0.1 g in 30 ml deionized water) was used as tungsten source and 0.12 sccm diethyl sulfide (DES) was used as sulfur source. For the growth of monolayer MoS_2 on *c*-plane sapphire substrate, ammonium molybdate (AMM) and KOH solution (0.43 g + 0.1 g in 30 ml deionized water) was used molybdenum source and 0.05 sccm DES was used as sulfur source. In the growth of $W_\alpha Mo_{1-\alpha}S_2$ alloy on *c*-plane sapphire substrate, the solution of AMT, AMM and KOH with Mo/W mole ratio of 1/2 was used as metal source and 0.05 sccm DES was as sulfur source. The alloy sample was transferred from sapphire to a SiO_2/Si substrate using a PMMA-assisted wet transfer method for 2D-HOM imaging. For *V*-doped monolayer WS_2 on SiO_2/Si, ammonium vanadate, AMT and KOH solution was used as metal source and 1.2 sccm DES was used as sulfur source. The mole ratios of $V/(V + W)$ in the metal solution were used to determine the nominal doping concentrations of *V* in the samples. Other growth parameters for the samples were identical. 1600 sccm Ar and 1 sccm H_2 were used as carrier gases. These Hy-MOCVD growths were completed in a 125 mm inner diameter tube furnace at 775 °C for 6 h.

The WSe_2 crystals were grown using a two-zone solid source CVD method. Before the growth process, 2 g of selenium (purity 99.999%, Thermo Fisher) was placed at the center of the first zone, while 8 mg of tungsten (VI) oxide (purity 99.995%, Sigma Aldrich) was placed in the second zone, which was positioned 30 cm away from the selenium boat. A 96 nm thick SiO_2 on Si substrate was then placed 5 cm downstream from the WO_3. The system was purged down to a base pressure of 10 mTorr before being raised to atmospheric pressure using Ar, and this pressure was maintained throughout the process. The temperature of the WO_3 and Se zones was set at 880 °C and 500 °C, respectively. The growth process was carried out for 40 min using a mixture of 25 sccm of Ar and 5 sccm of H_2. After the growth, the furnace was naturally cooled down to room temperature.

4.2. Preparation of WS_2/MoS_2 heterostructure

The WS_2/MoS_2 heterostructure was prepared by stacking MoS_2 film onto as-grown WS_2 triangles on a SiO_2/Si substrate, using a wet transfer method. The MoS_2 film separately grown on a sapphire substrate was spin-coated with PMMA, and then slowly dipped into deionized water. The MoS_2/PMMA layer was delaminated from sapphire by the deionized water and then transferred onto WS_2 as-grown on SiO_2/Si. The PMMA was removed by immersing the sample in acetone for 15 mins.

4.3. K-means cluster algorithm

The *K*-means clustering algorithm, implemented in the scikit-learn package [71], is designed to segregate 3D data into *n* specified clusters (C_1, C_2,…, C_n), with each cluster C_n containing a set of selected spectra with the number of m_n. In the 3D data generated by 2D-HOM, there are $x * y$ total spectra, each providing the reflectance information within the whole wavelength ranges, which have *P* variable-spectral points. Here, *x* and *y* represent the number of pixels of the 2D plane. The centroid of a cluster C_k is a point residing in a *P*-dimensional space, and it

is computed by averaging the values of each variable across the objects within that cluster. For instance, the centroid value for the jth variable in cluster C_n is calculated as follows:

$$\overline{x_j}^{(n)} = \frac{1}{m_n} \sum_{i \in C_n} x_{ij}.$$

And the centroid cluster of C_n is:

$$\bar{x}^{(n)} = \left(\overline{x_1}^{(n)}, \overline{x_2}^{(n)}, \ldots\ldots \overline{x_p}^{(n)}\right).$$

The standard k-means clustering algorithm functions through the following iterative procedure:

(1) The squared Euclidean distance between the ith object and the nth seed vector is obtained by $d^2(i, n) = \sum_{j=1}^{p} \left(x_{ij} - s_j^{(n)}\right)^2$.
(2) Following the initial allocation of hyperspectral spectra to clusters, compute the cluster centroid for each cluster. All the spectra are then compared to these centroids using the squared Euclidean distance $d^2(i, n)$. Each spectrum is moved to the cluster whose centroid is the closest, effectively reassigning spectra to the cluster with the most similar centroid.
(3) Using the updated cluster ID resulting from the previous step, determining the new centroid for each cluster by recalculating the centroids after all spectra have been reassigned to their respective clusters.
(4) Steps 2 and 3 are iteratively executed until no further changes occur in the composition of each cluster. In other words, this process is repeated until it converges, and each spectrum remains in its assigned cluster without further reassignment.

4.4. Materials characterization and analysis

Optical microscope images were taken using an Olympus BX-51 microscope in epi-reflection geometry. PL spectra were collected at room temperature using 532 nm laser excitation with a HORIBA Scientific LabRAM HR Evolution confocal microscope. DR images are generated by first selecting a nearby substrate region and averaging signal within it as $R_{\text{Substrate}}$ and then applying this value throughout the entire image to calculate the DR at each pixel. The DR curves are fitted with a single Lorentzian peak after subtracting a linear background. The PL curves are fitted by first subtracting a linear background and then performing a fit using a weighted Gaussian–Lorentzian function consisting of a blend of 55% Gaussian and 45% Lorentzian character. PL curves of 0%, 0.4%, 0.7% V-doped samples are fitted using 2 peaks and the higher energy peaks are chosen to calculate the Stokes shift. PL curves of 12%, 17%, 30% V-doped samples are fitted using 1 peak.

Data availability statement

The data that support the findings of this study are openly available at the following URL/DOI: https://doi.org/10.5281/zenodo.15128160 [72]. The code used in this article can be find in the Github page [73].

Acknowledgment

Primary support for this work was provided by the National Science Foundation Future of Semiconductors program (FuSe2, Award 2425218; Z.P., A.U., A.J.M., E.P.) and the Office of Naval Research Young Investigator Program (Award N000142512137; X.Z.). Sample growth received additional funding from the Stanford SystemX Alliance, sponsored by Taiwan Semiconductor Manufacturing Company (A.–T.H.). Early development was supported by the U.S. Department of Energy, Office of Basic Energy Sciences, under Contract DE–AC02–76SF00515 (Z.P., A.J.M.), and by instrumentation acquired under NSF MRI Award 2018008. Portions of this work were performed at the Stanford Nano Shared Facilities (SNSF, RRID: SCR_023230), supported by NSF Award ECCS–2026822.

Author contributions

Zhenghan Peng 0000-0002-4832-136X
Data curation (lead), Formal analysis (lead), Investigation (lead), Methodology (equal), Visualization (equal), Writing – original draft (equal), Writing – review & editing (equal)

Adeyemi Uthman 0009-0001-3701-0654
Data curation (supporting), Formal analysis (supporting), Investigation (equal), Methodology (equal), Visualization (equal), Writing – original draft (equal), Writing – review & editing (equal)

Zhepeng Zhang 0000-0002-9870-0720
Investigation (equal), Methodology (equal), Resources (equal), Writing – review & editing (supporting)

Anh Tuan Hoang 0000-0003-0911-1391
Investigation (supporting), Methodology (supporting), Resources (supporting), Writing – review & editing (supporting)

Xiang Zhu
Formal analysis (supporting), Writing – review & editing (supporting)

Eric Pop 0000-0003-0436-8534
Funding acquisition (supporting), Supervision (supporting), Writing – review & editing (supporting)

Andrew J Mannix 0000-0003-4788-1506
Conceptualization (lead), Funding acquisition (lead), Methodology (equal), Project administration (lead), Software (supporting), Supervision (lead), Writing – review & editing (supporting)

References

[1] Wang X, Cui Y, Li T, Lei M, Li J and Wei Z 2019 Recent advances in the functional 2D photonic and optoelectronic devices *Adv. Opt. Mater.* **7** 1801274
[2] Mak K F and Shan J 2016 Photonics and optoelectronics of 2D semiconductor transition metal dichalcogenides *Nat. Photon.* **10** 216–26
[3] O'Brien K P *et al* 2023 Process integration and future outlook of 2D transistors *Nat. Commun.* **14** 6400
[4] Das S *et al* 2021 Transistors based on two-dimensional materials for future integrated circuits *Nat. Electron.* **4** 786–99
[5] Turunen M, Brotons-Gisbert M, Dai Y, Wang Y, Scerri E, Bonato C, Jöns K D, Sun Z and Gerardot B D 2022 Quantum photonics with layered 2D materials *Nat. Rev. Phys.* **4** 219–36
[6] Quan J *et al* 2021 Phonon renormalization in reconstructed MoS_2 moiré superlattices *Nat. Mater.* **20** 1100–5
[7] Yuan L, Chung T-F, Kuc A, Wan Y, Xu Y, Chen Y P, Heine T and Huang L 2018 Photocarrier generation from interlayer charge-transfer transitions in WS_2-graphene heterostructures *Sci. Adv.* **4** e1700324
[8] Abbas G, Li Y, Wang H, Zhang W-X, Wang C and Zhang H 2020 Recent advances in twisted structures of flatland materials and crafting moiré superlattices *Adv. Funct. Mater.* **30** 2000878
[9] Kim Y, Woo W J, Kim D, Lee S, Chung S-M, Park J and Kim H 2021 Atomic-layer-deposition-based 2D transition metal chalcogenides: synthesis, modulation, and applications *Adv. Mater.* **33** e2005907
[10] Li T *et al* 2021 Epitaxial growth of wafer-scale molybdenum disulfide semiconductor single crystals on sapphire *Nat. Nanotechnol.* **16** 1201–7
[11] Tang A, Kumar A, Jaikissoon M, Saraswat K, Wong H-S P and Pop E 2021 Toward low-temperature solid-source synthesis of monolayer MoS_2 *ACS Appl. Mater. Interfaces* **13** 41866–74
[12] Zheng J, Yan X, Lu Z, Qiu H, Xu G, Zhou X, Wang P, Pan X, Liu K and Jiao L 2017 High-mobility multilayered MoS_2 flakes with low contact resistance grown by chemical vapor deposition *Adv. Mater.* **29** 1604540
[13] Kang K, Xie S, Huang L, Han Y, Huang P Y, Mak K F, Kim C-J, Muller D and Park J 2015 High-mobility three-atom-thick semiconducting films with wafer-scale homogeneity *Nature* **520** 656–60
[14] Hoang A T *et al* 2023 Low-temperature growth of MoS_2 on polymer and thin glass substrates for flexible electronics *Nat. Nanotechnol.* **18** 1439–47
[15] Aljarb A *et al* 2020 Ledge-directed epitaxy of continuously self-aligned single-crystalline nanoribbons of transition metal dichalcogenides *Nat. Mater.* **19** 1300–6
[16] Qin B *et al* 2024 Interfacial epitaxy of multilayer rhombohedral transition-metal dichalcogenide single crystals *Science* **385** 99–104
[17] Mannix A J *et al* 2015 Synthesis of borophenes: anisotropic, two-dimensional boron polymorphs *Science* **350** 1513–6
[18] Yoo M S, Byun K-E, Lee H, Lee M-H, Kwon J, Kim S W, Jeong U and Seol M 2024 Ultraclean interface of metal chalcogenides with metal through confined interfacial chalcogenization *Adv. Mater.* **36** e2310282
[19] Neilson K M *et al* 2024 Toward mass production of transition metal dichalcogenide solar cells: scalable growth of photovoltaic-grade multilayer WSe_2 by tungsten selenization *ACS Nano* **18** 24819–28
[20] Lin Y-T *et al* 2025 Photolithography-induced doping and interface modulation for high-performance monolayer WSe_2 P-type transistors *Nano Lett.* **25** 3571–8
[21] Tang J, He K, Lu P, Liang J, Guo K, Zhang Z, Wu R, Li B, Li J and Duan X 2025 Effect of fabricating process on the performance of two-dimensional p-type WSe_2 field effect transistors *Nano Lett.* **25** 1854–61
[22] Luo R, Gao M, Wang C, Zhu J, Guzman R and Zhou W 2024 Probing functional structures, defects, and interfaces of 2D transition metal dichalcogenides by electron microscopy *Adv. Funct. Mater.* **34** 2307625
[23] Rosenberger M R, Chuang H-J, Phillips M, Oleshko V P, McCreary K M, Sivaram S V, Hellberg C S and Jonker B T 2020 Twist angle-dependent atomic reconstruction and moiré patterns in transition metal dichalcogenide heterostructures *ACS Nano* **14** 4550–8
[24] Yang Y, Xu K, Holtzman L N, Yang K, Watanabe K, Taniguchi T, Hone J, Barmak K and Rosenberger M R 2024 Atomic defect quantification by lateral force microscopy *ACS Nano* **18** 6887–95
[25] Zhang K *et al* 2018 Tuning the electronic and photonic properties of monolayer MoS_2 via *in situ* rhenium substitutional doping *Adv. Funct. Mater.* **28** 1706950
[26] Dhakal K P, Duong D L, Lee J, Nam H, Kim M, Kan M, Lee Y H and Kim J 2014 Confocal absorption spectral imaging of MoS_2: optical transitions depending on the atomic thickness of intrinsic and chemically doped MoS_2 *Nanoscale* **6** 13028–35
[27] Havener R W, Kim C-J, Brown L, Kevek J W, Sleppy J D, McEuen P L and Park J 2013 Hyperspectral imaging of structure and composition in atomically thin heterostructures *Nano Lett.* **13** 3942–6
[28] Tebbe D, Schütte M, Kundu B, Beschoten B, Sahoo P K and Waldecker L 2023 Hyperspectral photoluminescence and reflectance microscopy of 2D materials *Meas. Sci. Technol.* **35** 035501
[29] Kolesnichenko P V, Zhang Q, Zheng C, Fuhrer M S and Davis J A 2021 Multidimensional analysis of excitonic spectra of monolayers of tungsten disulphide: toward computer-aided identification of structural and environmental perturbations of 2D materials *Mach. Learn.: Sci. Technol.* **2** 025021
[30] Zhang Z *et al* 2024 Chemically tailored growth of 2D semiconductors via hybrid metal-organic chemical vapor deposition *ACS Nano* **18** 25414–24
[31] Li Y and Heinz T F 2018 Two-dimensional models for the optical response of thin films *2D Mater.* **5** 025021
[32] Li Y, Chernikov A, Zhang X, Rigosi A, Hill H M, Van Der Zande A M, Chenet D A, Shih E-M, Hone J and Heinz T F 2014 Measurement of the optical dielectric function of monolayer transition-metal dichalcogenides: MoS_2, $MoSe_2$, WS_2, and WSe_2 *Phys. Rev. B* **90** 205422
[33] Ma E Y, Waldecker L, Rhodes D, Hone J, Watanabe K, Taniguchi T and Heinz T F 2020 High-resolution optical micro-spectroscopy extending from the near-infrared to the vacuum-ultraviolet *Rev. Sci. Instrum.* **91** 073107
[34] Niu Y *et al* 2018 Thickness-dependent differential reflectance spectra of monolayer and few-layer MoS_2, $MoSe_2$, WS_2 and WSe_2 *Nanomaterials* **8** 725
[35] Splendiani A, Sun L, Zhang Y, Li T, Kim J, Chim C-Y, Galli G and Wang F 2010 Emerging photoluminescence in monolayer MoS_2 *Nano Lett.* **10** 1271–5
[36] Mak K F, Lee C, Hone J, Shan J and Heinz T F 2010 Atomically thin MoS_2: a new direct-gap semiconductor *Phys. Rev. Lett.* **105** 136805

[37] Zhao W, Ghorannevis Z, Chu L, Toh M, Kloc C, Tan P-H and Eda G 2013 Evolution of electronic structure in atomically thin sheets of WS_2 and WSe_2 *ACS Nano* **7** 791–7
[38] Wang L *et al* 2017 Slow cooling and efficient extraction of C-exciton hot carriers in MoS_2 monolayer *Nat. Commun.* **8** 13906
[39] Kumar R, Verzhbitskiy I and Eda G 2015 Strong optical absorption and photocarrier relaxation in 2-D semiconductors *IEEE J. Quantum Electron.* **51** 1–6
[40] Qiu D Y, da Jornada F H and Louie S G 2013 Optical spectrum of MoS_2: many-body effects and diversity of exciton states *Phys. Rev. Lett.* **111** 216805
[41] Aleithan S H, Livshits M Y, Khadka S, Rack J J, Kordesch M E and Stinaff E 2016 Broadband femtosecond transient absorption spectroscopy for a CVD MoS_2 monolayer *Phys. Rev. B* **94** 035445
[42] Goswami T, Bhatt H, Babu K J, Kaur G, Ghorai N and Ghosh H N 2021 Ultrafast insights into high energy (C and D) excitons in few layer WS_2 *J. Phys. Chem. Lett.* **12** 6526–34
[43] Schmidt R, Niehues I, Schneider R, Drüppel M, Deilmann T, Rohlfing M, de Vasconcellos S M, Castellanos-Gomez A and Bratschitsch R 2016 Reversible uniaxial strain tuning in atomically thin WSe_2 *2D Mater.* **3** 021011
[44] Lin K-Q *et al* 2021 Narrow-band high-lying excitons with negative-mass electrons in monolayer WSe_2 *Nat. Commun.* **12** 5500
[45] Lin K-Q *et al* 2024 Ultraviolet interlayer excitons in bilayer WSe_2 *Nat. Nanotechnol.* **19** 196–201
[46] Loh L, Zhang Z, Bosman M and Eda G 2021 Substitutional doping in 2D transition metal dichalcogenides *Nano Res.* **14** 1668–81
[47] Zhang F *et al* 2020 Monolayer vanadium-doped tungsten disulfide: a room-temperature dilute magnetic semiconductor *Adv. Sci.* **7** 2001174
[48] Neamen D A 2003 *Semiconductor Physics And Devices: Basic Principles* 3rd edn (McGraw-Hill Science/Engineering/Math)
[49] Sasaki S, Kobayashi Y, Liu Z, Suenaga K, Maniwa Y, Miyauchi Y and Miyata Y 2016 Growth and optical properties of Nb-doped WS_2 monolayers *Appl. Phys. Express* **9** 071201
[50] Kumar V, Mishra R K, Kumar P and Gwag J S 2023 Electronic and optical properties of Nb/V-doped WS_2 monolayer: a first-principles study *Luminescence* **38** 1215–20
[51] Mak K F, He K, Lee C, Lee G H, Hone J, Heinz T F and Shan J 2013 Tightly bound trions in monolayer MoS_2 *Nat. Mater.* **12** 207–11
[52] Kolesnichenko P V, Zhang Q, Yun T, Zheng C, Fuhrer M S and Davis J A 2020 Disentangling the effects of doping, strain and disorder in monolayer WS_2 by optical spectroscopy *2D Mater.* **7** 025008
[53] Sousa F B, Zheng B, Liu M, Resende G C, Zhou D, Pimenta M A, Terrones M, Crespi V H and Malard L M 2024 Effects of vanadium doping on the optical response and electronic structure of WS_2 monolayers *Adv. Opt. Mater.* **12** 2400235
[54] Fan X, Siris R, Hartwig O, Duesberg G S and Niklaus F 2020 Rapid and large-area visualization of grain boundaries in MoS_2 on SiO_2 using vapor hydrofluoric acid *ACS Appl. Mater. Interfaces* **12** 34049–57
[55] van der Zande A M, Huang P Y, Chenet D A, Berkelbach T C, You Y, Lee G-H, Heinz T F, Reichman D R, Muller D A and Hone J C 2013 Grains and grain boundaries in highly crystalline monolayer molybdenum disulphide *Nat. Mater.* **12** 554–61
[56] Kim H W 2023 Recent progress in the role of grain boundaries in two-dimensional transition metal dichalcogenides studied using scanning tunneling microscopy/spectroscopy *Appl. Microsc.* **53** 5
[57] Wang D *et al* 2018 Bandgap broadening at grain boundaries in single-layer MoS_2 *Nano Res.* **11** 6102–9
[58] Kumar A, Xu L, Pal A, Agashiwala K, Parto K, Cao W and Banerjee K 2024 Strain engineering in 2D FETs: physics, status, and prospects *J. Appl. Phys.* **136** 090901
[59] Chaurasiya R, Dixit A and Pandey R 2018 Strain-mediated stability and electronic properties of WS_2, Janus WSSe and WSe_2 monolayers *Superlattices Microstruct.* **122** 268–79
[60] Chang C-H, Fan X, Lin S-H and Kuo J-L 2013 Orbital analysis of electronic structure and phonon dispersion in MoS_2, $MoSe_2$, WS_2, and WSe_2 monolayers under strain *Phys. Rev. B* **88** 195420
[61] Schauble K *et al* 2020 Uncovering the effects of metal contacts on monolayer MoS_2 *ACS Nano* **14** 14798–808
[62] Zhang X, Xiao S, Nan H, Mo H, Wan X, Gu X and Ostrikov K 2018 Controllable one-step growth of bilayer MoS_2–WS_2/WS_2 heterostructures by chemical vapor deposition *Nanotechnology* **29** 455707
[63] Wang G *et al* 2015 Spin-orbit engineering in transition metal dichalcogenide alloy monolayers *Nat. Commun.* **6** 10110
[64] Chen Y, Xi J, Dumcenco D O, Liu Z, Suenaga K, Wang D, Shuai Z, Huang Y-S and Xie L 2013 Tunable band gap photoluminescence from atomically thin transition-metal dichalcogenide alloys *ACS Nano* **7** 4610–6
[65] Miles C, Samajdar R, Ebadi S, Wang T T, Pichler H, Sachdev S, Lukin M D, Greiner M, Weinberger K Q and Kim E-A 2023 Machine learning discovery of new phases in programmable quantum simulator snapshots *Phys. Rev. Res.* **5** 013026
[66] Munkhbat B, Denis G B, Bisht A, Hoque M A, Karpiak B, Dash S P and Shegai T 2020 Electrical control of hybrid monolayer tungsten disulfide–plasmonic nanoantenna light–matter states at cryogenic and room temperatures *ACS Nano* **14** 1196–206
[67] Chakraborty B, Gu J, Sun Z, Khatoniar M, Bushati R, Boehmke A L, Koots R and Menon V M 2018 Control of strong light–matter interaction in monolayer WS_2 through electric field gating *Nano Lett.* **18** 6455–60
[68] Kopaczek J, Zelewski S, Yumigeta K, Sailus R, Tongay S and Kudrawiec R 2022 Temperature dependence of the indirect gap and the direct optical transitions at the high-symmetry point of the Brillouin zone and band nesting in MoS_2, $MoSe_2$, $MoTe_2$, WS_2, and WSe_2 crystals *J. Phys. Chem. C* **126** 5665–74
[69] Hill H M, Rigosi A F, Roquelet C, Chernikov A, Berkelbach T C, Reichman D R, Hybertsen M S, Brus L E and Heinz T F 2015 Observation of excitonic Rydberg states in monolayer MoS_2 and WS_2 by photoluminescence excitation spectroscopy *Nano Lett.* **15** 2992–7
[70] Kalinin S V, Ziatdinov M, Ahmadi M, Ghosh A, Roccapriore K, Liu Y and Vasudevan R K 2024 Designing workflows for materials characterization *Appl. Phys. Rev.* **11** 011314
[71] Pedregosa F 2011 Scikit-learn: Machine Learning in Python pp 2825–30 (available at: https://scikit-learn.org/stable/modules/clustering.html#k-means)
[72] Peng Z 2025 Data of Hyperspectral Optical Microscopy for Characterization of 2D Semiconductors and Heterostructures *Zenodo* (https://doi.org/10.5281/zenodo.15128160)
[73] Peng Z and Uthman A 2025 2D_Hyperspectral_Optical_Microscopy (available at: https://github.com/MannixGroup/2D_Hyperspectral_Optical_Microscopy)